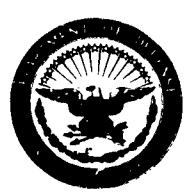

STANFORD RESEARCH INSTITUTE
MENLO PARK, CALIFORNIA

May 15, 1963

Progress Report No. 24
For the period February 1 to April 30, 1963

TUNGSTEN AND ROCKET MOTORS

SRI Project No. PMU 2785
Contract NOrd-18619

Prepared for:
Special Projects Office
Department of the Navy
Bureau of Naval Weapons
Washington 25, D. C.

Introduction

The current project, a continuation of Task II, NOrd-18619 concerns the use of tungsten in solid propellant rocket motors and involves two main areas of interest. The first area, tungsten erosion, is being studied under simulated exhaust conditions by means of a specially constructed plasma arc erosion apparatus. The second area deals with the effects of thermal shock on tungsten and includes an experimental study and theoretical analysis of the problem.

Erosion Studies

Al_2O_3 As Erodent

Preliminary results were given in the last progress report for the erosion of fg-pss* W in 280 grit Al_2O_3 (desiccator-stored) which had received no special drying treatment before injection into the argon plasma. The observed surface recession rate for the preliminary work was 0.024 mil sec^{-1} (2.4×10^{-5} inch sec^{-1}).

During the current reporting period specimens of both fg-pss W and Ag-infiltrated W were eroded with 280 grit Al_2O_3 which had been heated in vacuum at 1000°C for three hours to drive off surface contaminants. Colored motion pictures were taken in most runs. A quartz plate was placed 4 inches downstream from the specimen to collect solid erodent and solid erosion products for X-ray diffraction analysis. Also, samples of the exhaust gas were taken before and after introduction of Al_2O_3 to the plasma. The temperature on the plasma impingement surface of the W specimen was between 2250°C and 2500°C at the start of each run. Shortly after introduction of the Al_2O_3 the observed specimen

*Fine-grained, pressed, sintered and swaged.

Copy No. 10

temperature dropped by 150 to 300°C and then was relatively constant for the duration of the Al_2O_3 flow. The Al_2O_3 flowrate employed in most runs (130 mg sec^{-1}) was sufficient to keep a continuous film of Al_2O_3 flowing over the plasma impingement area. However, at higher flowrates the solidification of Al_2O_3 on cooler portions of the W specimen tended to interfere with projection of the specimen image. The duration of Al_2O_3 flow varied from 72 seconds for the shortest run to 796 seconds for the longest.

In no run did the 90-mil-diameter W rods erode more than 3 mils. The corresponding calculated surface recession rates ranged from 0.003 mil sec^{-1} to 0.028 mil sec^{-1}; all rates in this range represent relatively negligible erosion.

Observation of the projected specimen image during the run and later from the motion pictures revealed what appeared to be small quantities of W floating on certain regions of the molten Al_2O_3. After the run, these regions were darker than the remainder of the Al_2O_3 which had solidified on the tungsten specimen. X-ray diffraction analysis of this darkened material indicated only α-Al_2O_3 to be present. Thus, W was most likely present as only a thin layer on the molten Al_2O_3.

Metallographic examination and electron diffraction analysis of this darkened Al_2O_3 will be performed in the future. From comparison with previous results, it is felt that the W was transported through the molten Al_2O_3 and then redeposited at the Ar-Al_2O_3 surface. Whether this W transport occurred only from the cooler back face of the W specimen (as discussed in previous reports) or whether it also took place on the plasma impingement surface was not ascertained from the motion pictures.

The X-ray diffraction results on the quartz plates indicated that Al_2O_3 was deposited downstream from the fg-pss W specimens in every run. In the case of the Ag-infiltrated W, both Al_2O_3 and Ag were found after each run. Tungsten was also possibly present on the plate after some runs on both types of specimens (fg-pss and Ag-infiltrated). This could have been caused by the W transport in Al_2O_3 just described but might also have been due to W vaporizing from the specimen and depositing on the quartz plate. In any case, if and where W was present on the quartz plate it was only in very small quantities.

Mass spectrographic analysis showed no significant changes in composition of the exhaust gas after introduction of Al_2O_3 to either type of W specimen.

The relatively negligible erosion rates and the lack of observed reaction products for both fg-pss W and Ag-infiltrated W lead to the

conclusion that no appreciable erosion occurs under the conditions studied. What little reaction does take place seems to be connected with the transport of W through molten Al_2O_3.

CO_2 As Erodent

The erosion of fg-pss W and of Ag-infiltrated W in a CO_2-containing argon plasma were investigated. Colored motion pictures were taken of the projected specimen image in both experiments. Collection of solid and gaseous erosion products were performed by the same procedures as for the Al_2O_3 erosion studies.

The temperature on the plasma-impingement surface of the specimen just before introduction of the CO_2 was 2435°C for both experiments. In both cases an approximately linear decrease in specimen temperature was noted as the erosion proceeded. This was attributed to differences in over-all heat transfer to and from the specimen caused by the reduced section resulting from erosion. The CO_2 flowrate in both experiments was 22 mg sec^{-1}.

The maximum diametrical recession on the specimens was measured on enlargements of single frames from the motion pictures. These results are plotted versus time in Figs. 1 and 2. For the fg-pss W (Fig. 1) a very linear recession rate (.39 mil sec^{-1}) is observed to start somewhere between 20 and 60 seconds after the CO_2 was introduced, and to continue until the specimen had eroded to approximately one-half its initial diameter. In the case of the Ag-infiltrated W (Fig. 2) the change in diameter with time is much less smooth than for the fg-pss W. It does, however, become approximately linear (.42 mil sec^{-1}) after the first 10 to 20 seconds.

The non-linear recession at the beginning of both Figs. 1 and 2 is attributed to the system attempting to achieve quasi-steady-state conditions. This was not noticed in earlier similar work (see Progress Report No. 22) on cg-pss* W because the image projection and photographic techniques were less refined. The difference in linear recession rate between the two materials is small, in fact is less than the maximum error in their determination. These rates are somewhat higher than those reported earlier for both fg-pss W and Ag-infiltrated W, probably because the results from the earlier recession rates were averaged over a one-minute experiment and would thus include whatever slow nonlinear recession might occur in the early part of the run.

In the case of the Ag-infiltrated W another contributing factor is probably present. The earlier work reported a surface recession rate of 0.23 mil sec^{-1} for Ag-infiltrated W which had been eroded for 60 seconds in CO_2. In that work it was possible to heat the specimen for

*Coarse grained, pressed, sintered and swaged.

only 7 seconds before introduction of the CO_2. In the present work, however, it was necessary to heat the Ag-infiltrated W for 2-1/2 minutes in the argon plasma before introduction of the CO_2 in order to focus the specimen image, adjust the pyrometer, and take the initial gas sample. During this period a significant quantity of Ag was observed to leave the specimen. By the time the CO_2 was introduced, the apparent rate of Ag loss had appreciably decreased. Thus, any inhibiting effect of the Ag on erosion by CO_2 would have less effect on the results shown in Fig. 2 than in the low erosion rate (0.23 mil sec^{-1}) reported earlier. It therefore seems that Ag probably does inhibit the erosion of W by CO_2 but only to a small degree.

As for erosion mechanisms, the X-ray diffraction results of the quartz plate sample showed only WO_3 present for the fg-pss W run while both Ag and WO_3 were found for the experiment with Ag-ilfiltrated W. The gas sample bottles for both runs had sizable air leaks and although no change in gas constituents other than the presence of CO_2 was observed, small quantities of gaseous reaction products may have escaped detection. It is concluded that the mechanism for the erosion of fg-pss W and Ag-infiltrated W by an argon plasma into which CO_2 has been injected is the oxidation of W to WO_3.

CO As Erodent

The erosion of fg-pss W in an argon plasma containing CO was studied. The specimen temperature was 2260°C just prior to CO injection. It dropped to 2150°C shortly thereafter and was essentially constant throughout the remainder of the run. The CO flowrate employed was 18 mg sec^{-1}. The duration of CO flow was approximately 3 minutes.

The maximum diametrical recession measured after the run was only 2 mils. This represents negligible erosion for a 3-minute exposure time. No reaction products were detected by X-ray diffraction analysis of the quartz plate sample. Analysis of the gas samples showed no significant increase in CO_2 or other likely reaction products after injection of the CO. These results lead to the not surprising conclusion that W does not appreciably erode in CO for the conditions studied. At higher temperatures, however, significant erosion through the formation of W carbides is possible. This topic is discussed in the next paragraphs.

At first glance, it would seem desirable to keep the CO to CO_2 ratio in the rocket exhaust as high as possible in order to reduce the amount of W erosion caused by the reaction:

$$W(s) + 3CO_2(g) \rightarrow WO_3(g) + 3CO(g) \qquad (1)$$

If the ratio is made too high, however, one of the W carbides may form. This would be deleterious because the carbides have considerably lower melting points than W. Just such a formation was observed in earlier project work[1] on the static-system reactions of W with CO at high

pressures. The various experiments performed in the earlier work are shown in Table I. The reaction zone on the specimen from run 247 was determined by X-ray diffraction analysis to consist of W and large quantities of α-W_2C. No indication of WC was noted.

It can be observed from Table I that as the CO pressure was increased in each succeeding run at 2500°C (runs 244 through 247) the amount of W_2C formed (weight gain) increased. A similar trend was not observed when the temperatures were increased while employing a CO pressure of approximately 300 psi (runs 246, 248, 249). It is thus concluded that in these temperature and pressure ranges the rate of W_2C formation is probably more pressure-dependent than temperature-dependent.

Melting through the specimen was observed in the runs at 3150 and 3200°C. This is attributed either to melting of W_2C (melting point[2] somewhat above 2800°C) or to the formation of still lower melting liquid of composition between W and W_2C. In any case, this premature melting is illustrative of the possible dangers in exposing W to CO at high temperatures and pressures.

Two possible chemical reactions were considered for the formation of W_2C from W and CO:

$$4W(s) + 2CO(g) \rightarrow 2W_2C(s) + O_2(g) \qquad (2)$$

$$\text{and } 2W(s) + 2CO(g) \rightarrow W_2C(s) + CO_2(g) \qquad (3)$$

The free energies of each reaction $[\Delta F_{2500^\circ C}]_{R_X}$ were calculated for the conditions at the end of run 247 from the relation

$$[\Delta F_{2500^\circ C}]_{R_X} = [\Delta F^\circ_{2500^\circ C}]_{R_X} + RT \ln \frac{a_3 a_4}{a_1 a_2} \qquad (4)$$

where R_X = reaction No. X

a_1, a_2 = activities of the reactants

a_3, a_4 = activities of the reaction products

The $\Delta F_{2500^\circ C}$ values for CO and CO_2 were obtained from reference 3. Very little thermodynamic data are available for W_2C, and to obtain the required $\Delta F^\circ_{2500^\circ C}$ it was assumed that $\Delta S^\circ \neq f(T)$. The $\Delta F^\circ_{25^\circ C}$ and $\Delta S^\circ_{25^\circ C}$ values used were from reference 4. The resulting $\Delta F_{2500^\circ C}$ figures for reactions (2) and (3) were

$$[\Delta F_{2500^\circ C}]_{R_{(2)}} = +27 \text{ Kcal/mol CO} \qquad (5)$$

$$[\Delta F_{2500^\circ C}]_{R_{(3)}} = -3 \text{ Kcal/mol CO} \qquad (6)$$

Although these figures may be somewhat in error because of the necessary assumption that $\Delta S^\circ_{W_2C} \neq f(T)$, the free energy of reaction (3) is appreciably more negative than that of reaction (2) for the conditions at the end of run 247. Therefore, reaction (3) is considered to have been operative.

It is of interest that in reaction (3), CO goes to CO_2; while in the oxidation reaction (1) that was to be suppressed by increasing the CO to CO_2 ratio, CO_2 goes to CO. Thus, in a closed system composed only of W, CO, and CO_2, it would seem that if the CO to CO_2 pressure ratio or some similar function were increased above some value, W_2C would begin to form and if it were decreased below some other value WO_3 would form. This function may be calculated for reaction (3) by assuming that the equilibrium partial pressures represent the minimum condition for W_2C formation. From equation (4), at equilibrium, and assuming the activities of the gaseous components equal to the pressures, and the activities of W and W_2C equal to 1,

$$[\Delta F_{2500^\circ C}]_{R_{(3)}} = 0 = [\Delta F^\circ_{2500^\circ C}]_{R_{(3)}} + RT \ln \frac{P_{CO_2}}{(P_{CO})^2} \qquad (7)$$

and using the same $\Delta F^\circ_{2500^\circ C}$ values described earlier

$$[\Delta F^\circ_{2500^\circ C}]_{R_3} = 24 \text{ Kcal/mol CO} \qquad (8)$$

$$\frac{(P_{CO_2})^2}{P_{CO_2}} \text{ for reaction (3)} = 6.3 \times 10^3 \text{ atm} \qquad (9)$$

This value of the pressure ratio function is plotted on logarithmic coordinates in Fig. 3. It is seen that the resulting straight line is a boundary between CO and CO_2 pressure regions in which W_2C is stable and unstable. Also plotted in Fig. 3 are the equilibrium partial pressures of $WO_3(g)$ (obtained from reference 5) for reaction (1) at various values of CO/CO_2 in order to give some idea of the extent of reaction (1) in these same pressure regions. Although all the information given by Fig. 3 is for equilibrium conditions and is calculated from approximate thermodynamic data, and although a rocket exhaust nozzle environment is not necessarily at equilibrium, the results illustrate the following point: While increasing the CO to CO_2 ratio drastically reduces the amount of $WO_3(g)$ formation (and consequent loss of W) it can result in W_2C formation if made too great. Also, the equilibrium values in Fig. 3 give some quantitative idea of the pressure ranges where both formations are important.

The P_{CO} versus P_{CO_2} values in both the chamber and throat for an unclassified NP propellant are also included in Fig. 3 as an example of a pressure range corresponding to a rocket exhaust nozzle.

Thermal Shock Study

A fourth series of pressed and sintered tungsten cylinders (90% dense) was completed and sent to Aerojet-General Corporation, Azusa, for mechanical property testing, as described in earlier reports. Testing has begun on the property determinations and the results will be reported as soon as available.

A series of screening tests were made during this report period on various types of tungsten. In conjunction with these screening tests, the thermal shock apparatus, as described in previous reports, was slightly modified so that a water "heat sink" could be flowed over the outside specimen surface during a test run. The water flow reduces the rate of temperature rise on the specimen O.D. and consequently increases the maximum attainable thermal gradient for a given heat flux. It also minimizes any surface oxidation and thus facilitates the inspection for thermal shock cracks after the run.

Most specimens were tested using the water "heat sink" but a few were tested without it and, as will be shown later, thermal shock cracking was observed to occur in both cases. The materials investigated were silver-infiltrated tungsten. The wrought and the recrystallized samples were supplied and tested on another project, but some of the data is presented here because it is of general interest. The silver-infiltrated samples were supplied by and tested for Aerojet-General Corporation, Sacramento. They were taken from billets received by various vendors and represent different processing procedures.

The specimen outer surface temperature and circumferential strain were measured during each test run. In addition, the graphite heater temperature was recorded. The heater thermal history (heater surface temperature versus time) during a typical test run is given for wrought or recrystallized tungsten in Fig. 4 and for silver-infiltrated tungsten in Fig. 5. The variation in the maximum heater temperature attained for the various runs is also indicated on the figures.

The thermal shock test results for wrought and recrystallized tungsten are summarized in Table II, and for silver-infiltrated tungsten in Table III. They will be discussed in terms of tungsten type.

Wrought Tungsten

A typical thermal stress versus time plot is shown in Fig. 6 for a wrought tungsten cylinder (Specimen 5, Table II) tested in the thermal shock apparatus. As may be seen, the calculated*

*The stress was calculated (using experimentally determined strain and temperature data) by means of the relationships developed and described in previous progress reports.

outer circumferential stress rises very rapidly to 114,000 psi after 7 seconds. Simultaneously, the ultimate tensile strength drops (due to increasing O.D. temperature) to a value of 105,000 psi. The strain rate at 7 seconds was 0.1 min^{-1} and the O.D. temperature was about 950°F. The specimen emitted audible cracking noises after about 6.5 seconds. Examination of Specimen 5 after the run revealed both circumferential and radial cracks (Fig. 7).

Using the previously described thermal shock test, a total of seven wrought specimens were tested. All specimens were inspected by fluorescent dye penetrant techniques before testing and no flaws were detected. As may be seen in Table II, the use or absence of a water "heat sink" appeared to have no significant effect on the incidence of thermal shock cracking. However, as will be shown below, the variation between different types of wrought tungsten did appear significant.

Forged Tungsten --The forged samples appeared particularly susceptible to circumferential cracking (Fig. 7, and Table II). These cracks initiated on the outer surface and propagated inward to various depths ranging from a few mils to the entire wall thickness. A photomicrograph (Fig. 8) of a polished radial section of Specimen 2a, Table II, shows a typical circumferential crack.

In addition to circumferential cracking, one of the three forged specimens (Specimen 5, Fig. 7) had radial edge cracks which were quite shallow.

Forged and Ground Tungsten. -- One forged specimen (No. 1a, Table II) had been ground on the O.D. and I.D. surfaces by the supplier. Unlike the unground forgings, no circumferential cracks were noted in this specimen after thermal shock testing. It is possible that the grinding eliminated or minimized surface notches such as machining marks which might act as stress raisers and lead to circumferential crack initiation. However, radial edge cracks did occur on one of the unground ends, Fig. 9. These radial cracks appear to be I.D. initiated and may have propagated from grinding micro-cracks already present.

Spun Tungsten. -- The shear spun cylinders tested were more resistant to circumferential thermal shock cracking than the forged material, Table II. No circumferential cracks were noted in any of the three "as-spun" specimens. One specimen did possess two radial cracks, however, which were quite severe. One of these cracks propagated through the entire wall thickness, Fig. 10.

The wrought structures of the spun tungsten and forged tungsten specimens were examined metallographically. The spun material (Fig. 11) had a pronounced grain elongation parallel to the cylinder axis, whereas the forged tungsten had a relatively homogeneous structure with possibly a slight grain elongation in the circumferential direction (Fig. 12). In each case thermal shock cracking occurred predominantly in a direction parallel to the grain flow, i.e., radially in the spun

tungsten and circumferentially in the forged material, indicating that there may be a correlation between structural anisotropy and thermal shock resistance. However, more data must be obtained before any firm conclusions can be made.

Recrystallized Tungsten

Recrystallization of tungsten results in a reduction of anisotropy with respect to strength properties and ductility. It also leads to an appreciable decrease in tensile strength and to an increase of the ductile-brittle transition temperature; both of these factors should result in a reduction of the thermal shock resistance.

Lowered thermal shock resistance was particularly noticeable for as-spun and recrystallized tungsten. Unlike the more resistant as-spun tungsten, the recrystallized material (Specimen 7, Table II) developed both radial and circumferential cracks (Fig. 13). The radial cracks formed only at one end of the specimen and each crack had several branches. The average radial crack length in the axial direction was about 1/4 inch. The circumferential stress versus time plot for this specimen is shown in Fig. 14. As may be seen in the figure, the ultimate tensile strength was exceeded after about 5-1/2 seconds at a strain rate of about 0.1 min^{-1}. The outer surface temperature at this time was 620°F.

As-forged and recrystallized tungsten also exhibited poor thermal shock resistance. The one specimen tested (Specimen 4, Table II) developed a severe radial crack which propagated across the cylinder wall and along the entire specimen length. Once this crack had formed, the circumferential stress was relieved and the axial stress reduced. This reduction in axial stress is probably the reason that no circumferential cracks were noted in this specimen.

Silver-Infiltrated Tungsten

The infiltration of tungsten by silver under proper processing conditions might well be expected to improve thermal shock resistance. Silver additions increase the thermal conductivity and the low temperature strength of tungsten over that of the pressed and sintered material without appreciably raising the elastic modulus or thermal expansion coefficient. All of these factors should lead to increased thermal shock resistance.

The silver-infiltrated specimens tested to date were of a different size from the wrought specimens and therefore no direct comparisons can be made between the two types of tungsten. However, it is possible to compare the relative thermal shock resistance of each of the ten infiltrated specimens, and to correlate this with the material properties and pretest inspection results. The thermal shock test results for the ten infiltrated specimens are summarized in Table III. A thermal stress

versus time plot is presented in Fig. 15 for a typical specimen (Ag-7, Table III). As may be seen, the outer circumferential stress (σ_θ) rises rapidly to a value of 53,000 psi in about 8.3 seconds. At this time, the ultimate tensile strength at the temperature of the outer surface (730°F) was about 56,000 psi. An audible cracking noise was emitted from the specimen at about 8 seconds and a severe radial crack (Fig. 16) was observed after the run.

O.D.-initiated thermal shock cracks were observed in three of the ten specimens tested (Table III). In a fourth specimen, an I.D. crack network was observed (Fig. 17). It is not known whether these I.D. initiated cracks occurred on heating or after the run on cooling. It is possible to generate I.D. tensile stresses during a run due to plastic upset in the initial portion of the test[7] but it is difficult to see how these stresses could lead to cracking at the very hot I.D. surface. As may be seen in Table III, there is good correlation between flaws detected by pretest inspection at Aerojet-General and actual thermal shock cracking in three of the four specimens exhibiting post-test cracks. It thus appears, as would be expected, that a homogeneous flaw-free material is essential for satisfactory thermal shock resistance.

Gerald M. Gordon
Senior Metallurgist

David A. Brown
Metallurgist

Approved:

A. E. Gorum, Director
Material Sciences Division

REFERENCES

1. A. Neiman, et al. "Tungsten and Rocket Motors," Final Report, Contract No. NOrd-18619(FBM), March 23, 1961.

2. E. K. Storms. "A Critical Review of Carbides--Part I," LAMS-2674 (1962).

3. L. S. Darken and R. W. Gurry. "Physical Chemistry of Metals," McGraw-Hill (1953).

4. I. E. Campbell (Editor). "High Temperature Technology," Wiley, New York (1956).

5. Atlantic Research Corp. "Gas-Metal Reactions in Rocket Nozzles," ASD-TDR 62-327, Part I June (1962).

6. W. H. Jones and L. J. Delaney. "An Analysis of the Materials Problem for Throat Inserts of High Energy Solid Propellant Rockets," Institute for Defense Analyses, Technical Report No. 62-19.

7. I. Vigness. "Thermal Stress Transients in Nozzles," Tech. Memo 157, NRL Project 62R05-19B, June 1961.

Table I

EXPERIMENTS ON REACTIONS BETWEEN W AND CO AT HIGH PRESSURES IN A STATIC SYSTEM*

Run No.	Temp. °C	Avg. CO Pressure psi	Reaction Time min	Wgt. Gain On Specimen mg
244	2500	40	2	0
245	2500	102	2	0.1
246	2500	292	2	0.8
247	2500	924	2	4.4**
248	2750	298	2	1.1
249	3000	309	2	0.4
250	3150	316	2	specimen melted
251	3200	290	0.58	specimen melted

*Data from Reference 3.

**X-ray diffraction indicated definite formation of W_2C, no WC noted.

Table II

THERMAL SHOCK TEST SUMMARY OF WROUGHT TUNGSTEN AND RECRYSTALLIZED TUNGSTEN

Specimen Number	Dimensions (inches) I.D.	O.D.	Height	Wall Thickness	Surface Finish	Water Heat Sink Used	Cracking Noted After Run: Radial Cracks	Cracking Noted After Run: Circumferential Cracks
As-Forged Tungsten								
2a	2.39	2.52	1.0	.065	as-machined	No	-	severe
2b	2.39	2.52	1.0	.065	as-machined	Yes	-	moderate
5	2.23	2.42	1.0	.108	as-machined	Yes	minor	severe
As-Forged and Ground on I.D. and O.D. Surfaces								
1a	2.20	2.43	1.0	.104	as-ground	Yes	moderate (one end)	-
As-Spun Tungsten								
6	2.23	2.44	1.0	.101	as-spun	Yes	-	-
8	2.27	2.49	1.0	.104	as-spun	Yes	-	-
9	2.23	2.46	1.0	.103	as-spun	No	severe	-
As-Forged and Recrystallized (1/2 hr at 2600°F)								
4	2.22	2.42	1.0	.102	as-machined	No	severe	-
As-Spun and Recrystallized (1/2 hr at 2600°F								
7	2.25	2.48	1.0	.107	as-spun	Yes	severe	severe

Table III

THERMAL SHOCK TEST SUMMARY OF SILVER-INFILTRATED TUNGSTEN
(all specimens 3/4" I.D. x 1-1/2" O.D. x 2" long)

Spec. No.	Vendor	Water Heat Sink Used	Flaws Detected by Pretest Inspection	Skeleton Density (g/cc)	Infiltrated Density (g/cc)	Cracking Noted After Run: Radial	Cracking Noted After Run: Circumferential
1	Fansteel	Yes		14.81	17.04	-	-
2	Sylvania	Yes		14.98	16.98	-	-
3	Kennemetal	Yes	defective material	14.2	16.7	moderate	-
4	Wah Chang	Yes		-	-	-	-
5	Wah Chang	Yes	structural defect present	-	-	severe[1]	moderate[1]
6	General Electric	Yes				-	-
7	General Electric/P. R. Mallory	Yes	wide density variation on micro basis	-	17.13	severe	-
8	Firth Sterling	Yes		16.05	17.65	-	-
9	Firth Sterling	No		16.08	17.61	moderate	minor
10[2]	Firth Sterling	No		16.0	17.69	possible minor (surface heat check network)	possible minor (surface heat check network)

1. These cracks appear to have initiated on the inside cylinder surface.
2. This specimen was infiltrated with sterling silver.

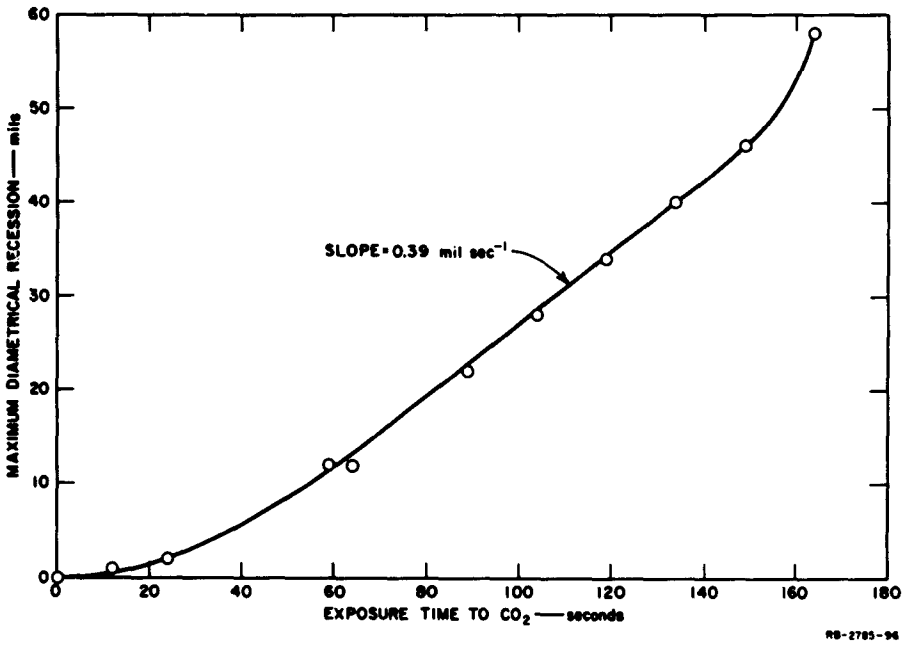

FIG. 1 RECESSION vs. TIME OF fg-pss W IN CO_2

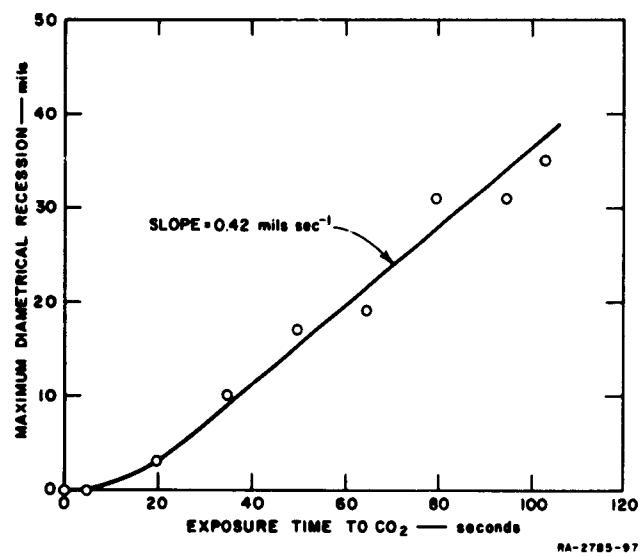

FIG. 2 RECESSION vs. TIME OF SILVER-INFILTRATED W IN CO_2

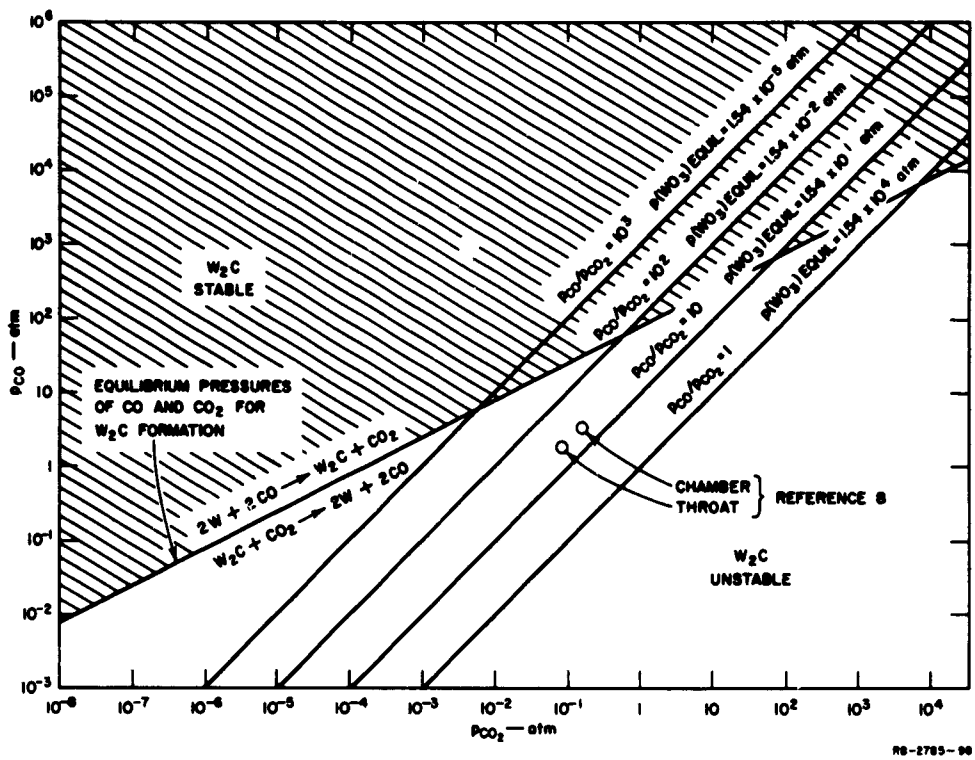

FIG. 3 EQUILIBRIUM PRESSURES OF CO AND CO_2 FOR W_2C AND WO_3 FORMATION

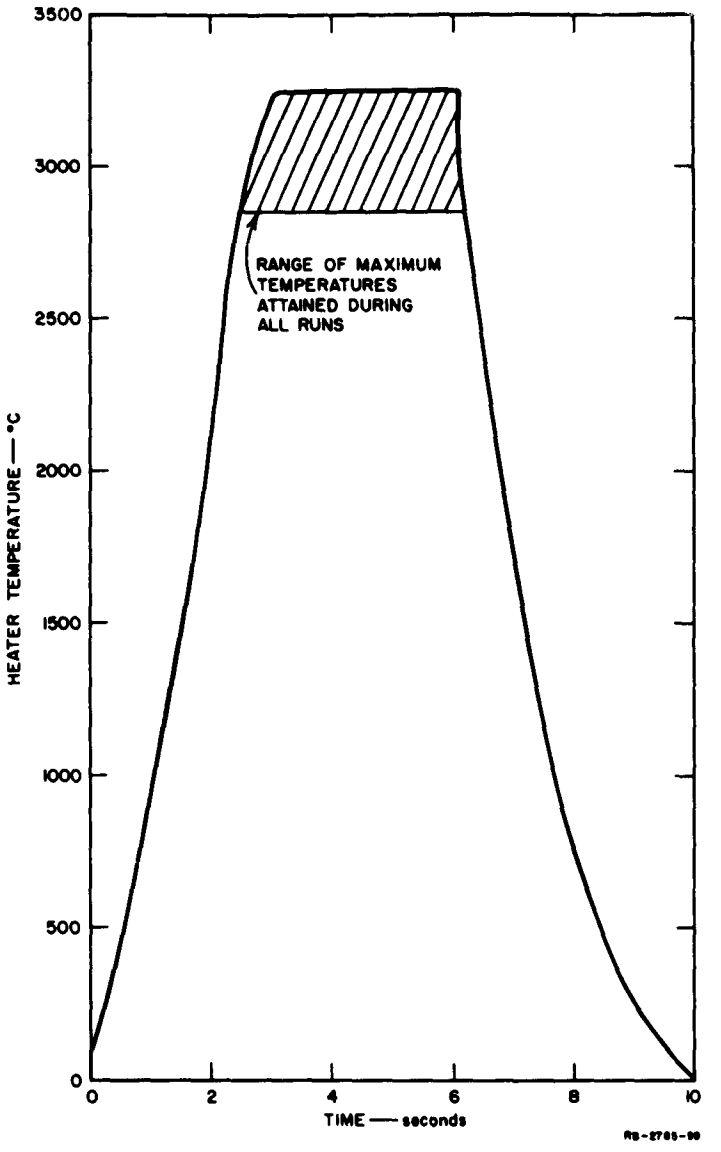

FIG. 4 TYPICAL HEATER TEMPERATURE HISTORY FOR THERMAL SHOCK RUNS ON WROUGHT OR RECRYSTALLIZED TUNGSTEN

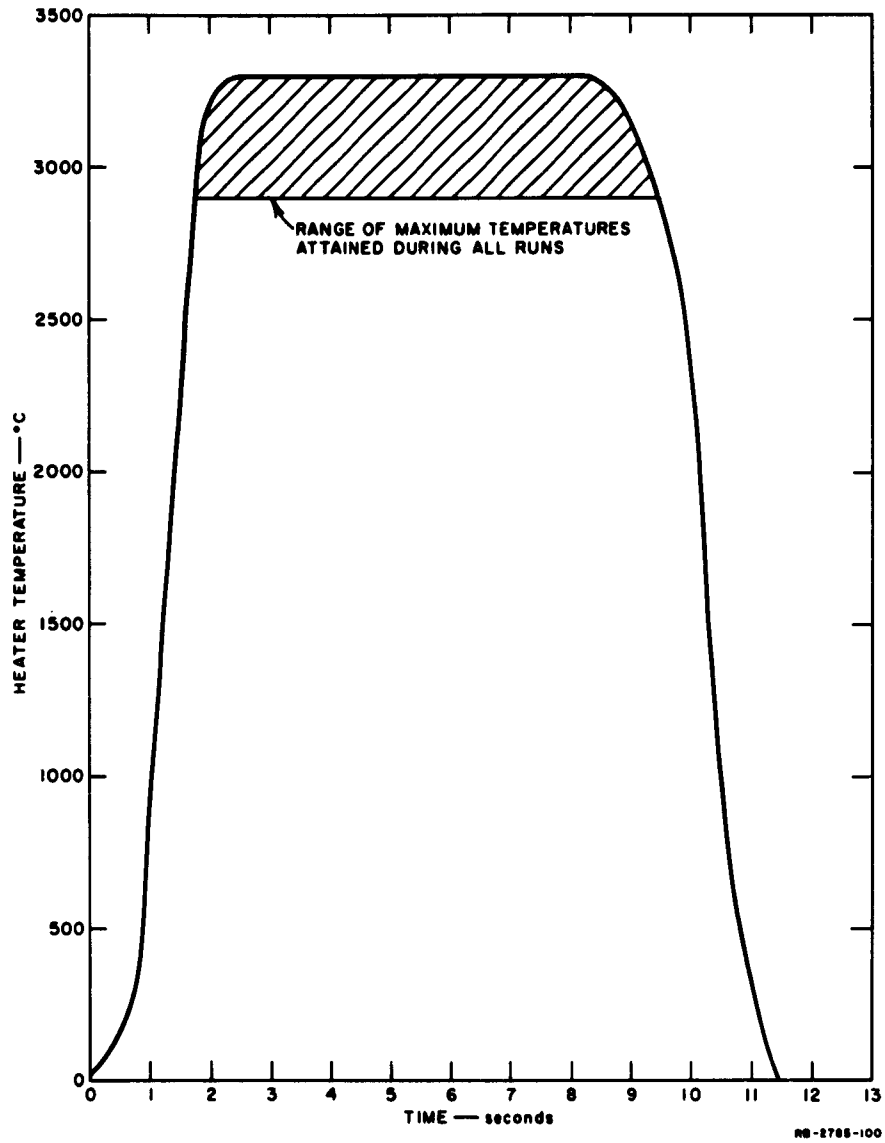

FIG. 5 TYPICAL HEATER TEMPERATURE HISTORY FOR THERMAL SHOCK RUNS ON SILVER-INFILTRATED TUNGSTEN

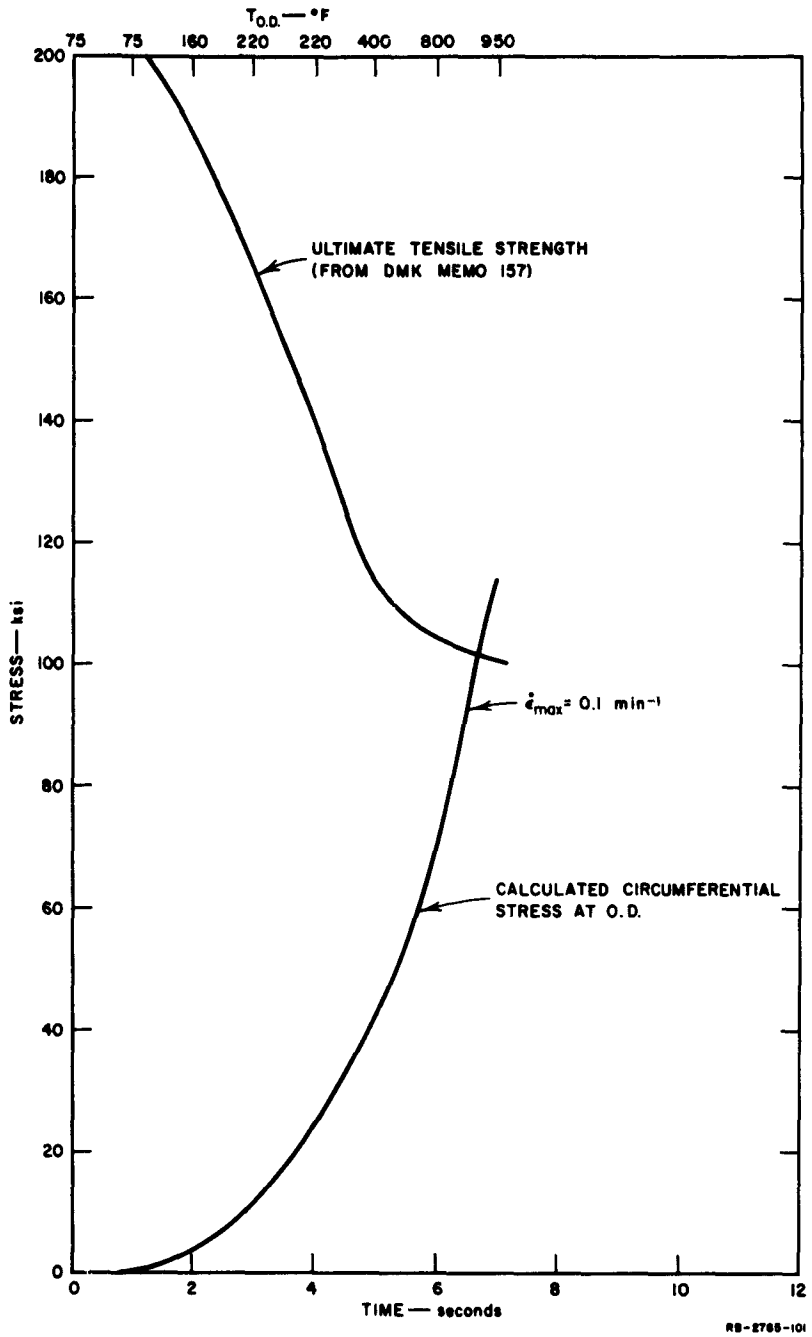

FIG. 6 STRESS AT OUTER SURFACE OF FORGED TUNGSTEN CYLINDER (No. 5) vs. TIME AND O.D. TEMPERATURE

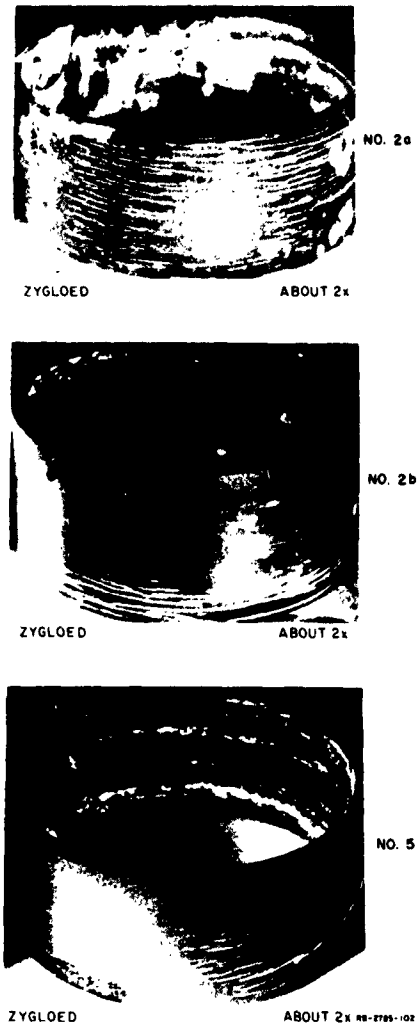

FIG. 7 FORGED TUNGSTEN SPECIMENS SHOWING THERMAL SHOCK CRACKS

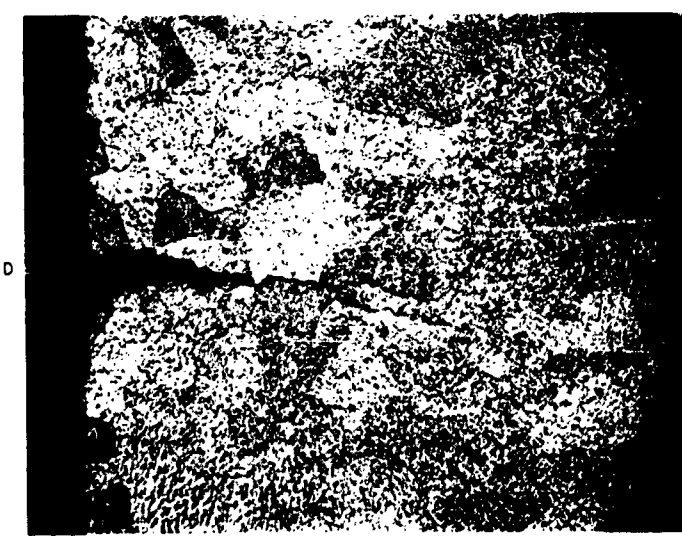

FIG. 8 MAGNIFIED RADIAL SECTION SHOWING TYPICAL CIRCUMFERENTIAL CRACK

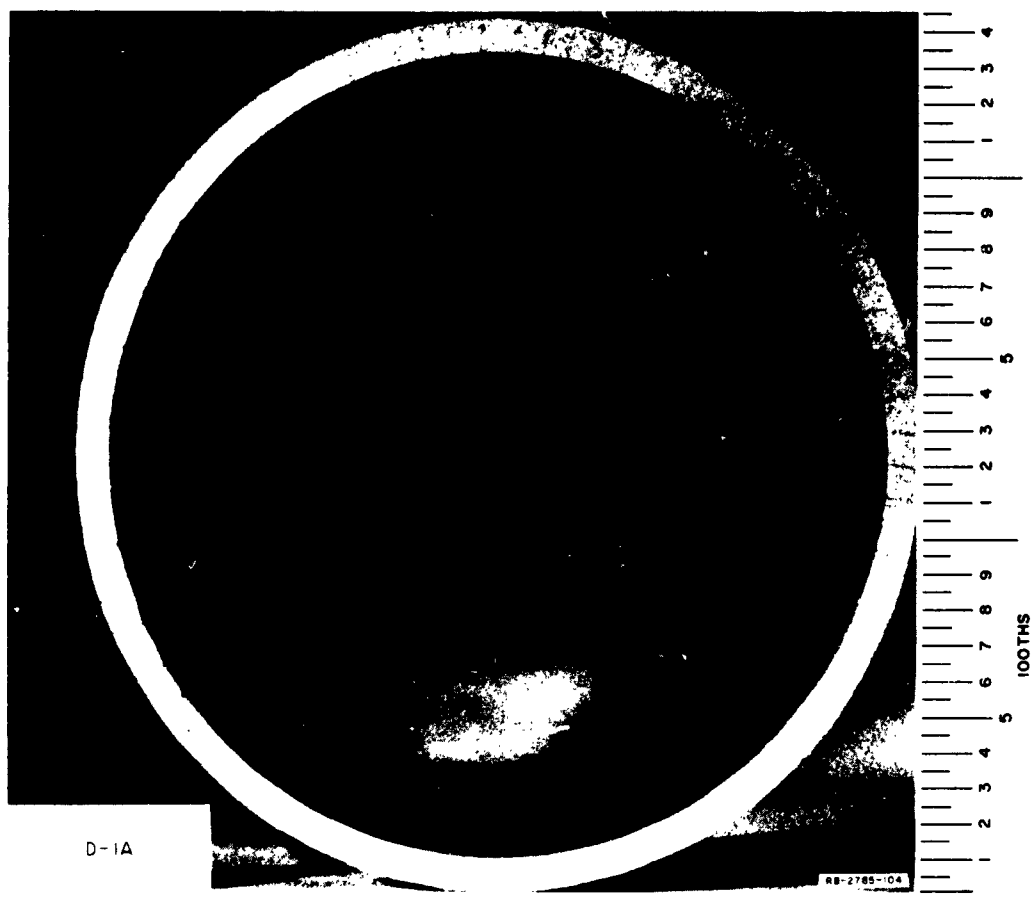

FIG. 9 FORGED AND GROUND SPECIMEN (No. 1a) SHOWING SHALLOW RADIAL THERMAL SHOCK CRACKS AT ONE END

FIG. 10 SHEAR SPUN SPECIMEN (NO. 9) SHOWING RADIAL THERMAL SHOCK CRACK

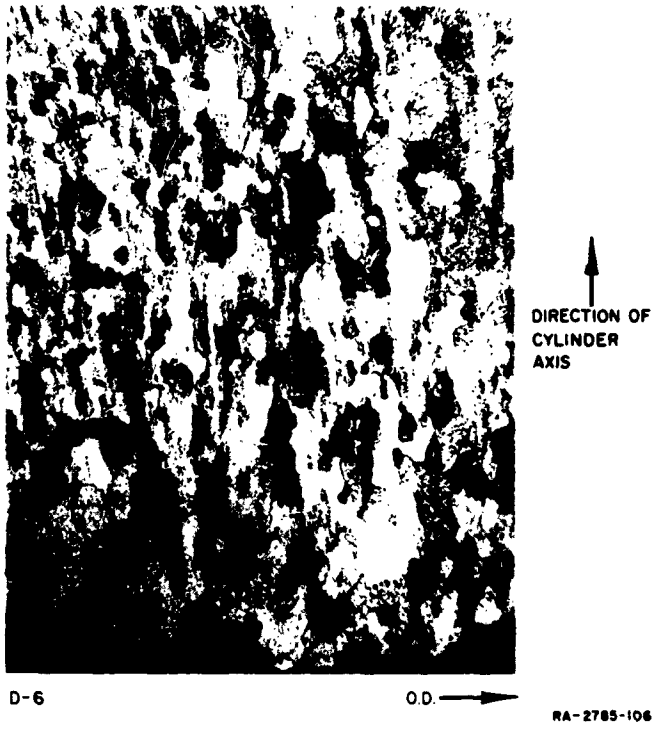

FIG. 11 RADIAL SECTION THROUGH SPUN TUNGSTEN SPECIMEN (No. 6) SHOWING GRAIN ELONGATION

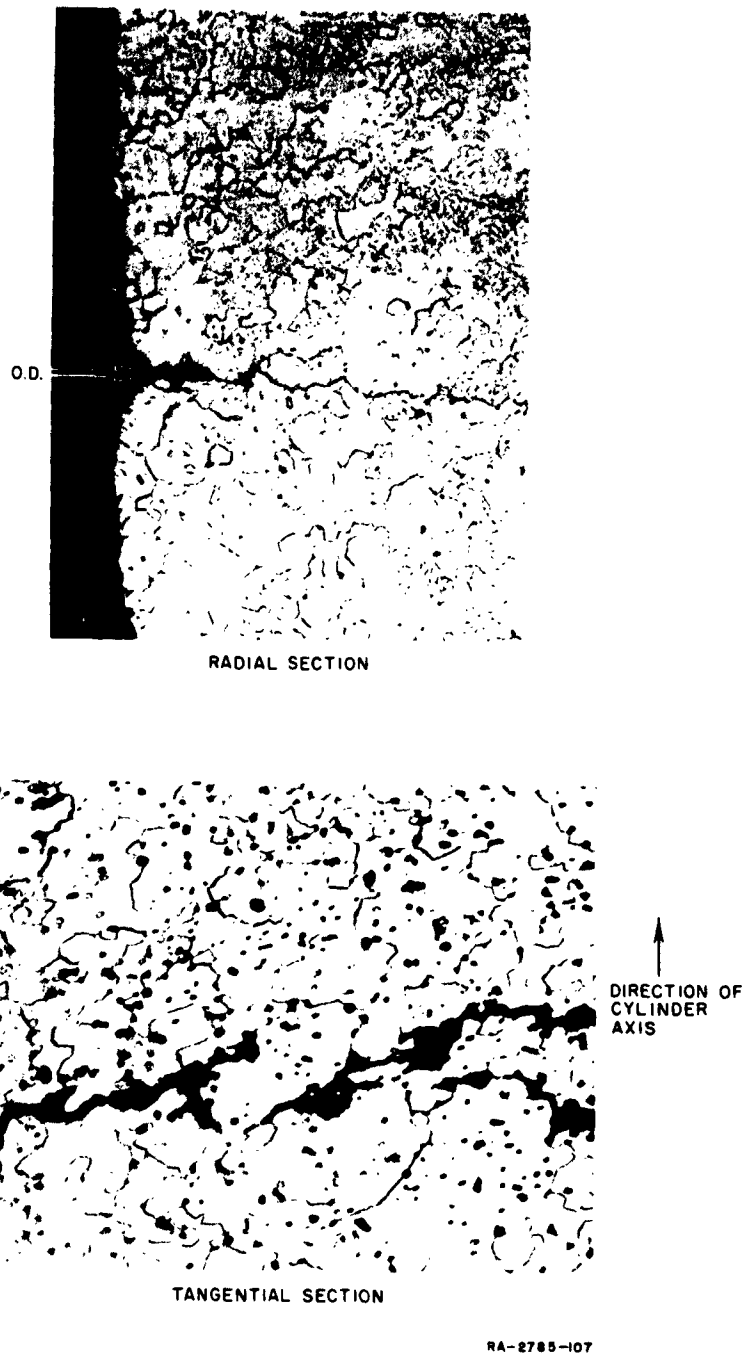

FIG. 12 SECTIONS OF FORGED TUNGSTEN SPECIMEN (No. 5) SHOWING CIRCUMFERENTIAL THERMAL SHOCK CRACK

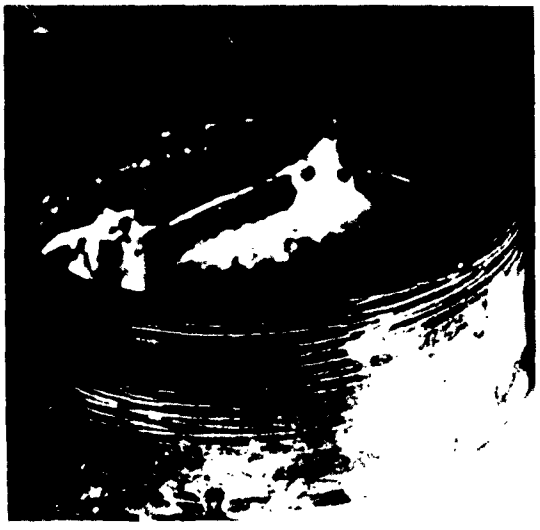

ZYGLOED ABOUT 1-1/2x

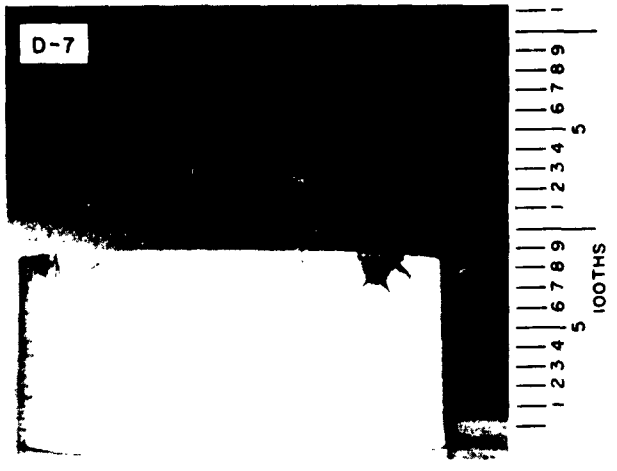

RA-2785-109

FIG. 13 AS-SPUN AND RECRYSTALLIZED TUNGSTEN SPECIMEN (D-7) SHOWING BOTH RADIAL AND CIRCUMFERENTIAL THERMAL SHOCK CRACKS

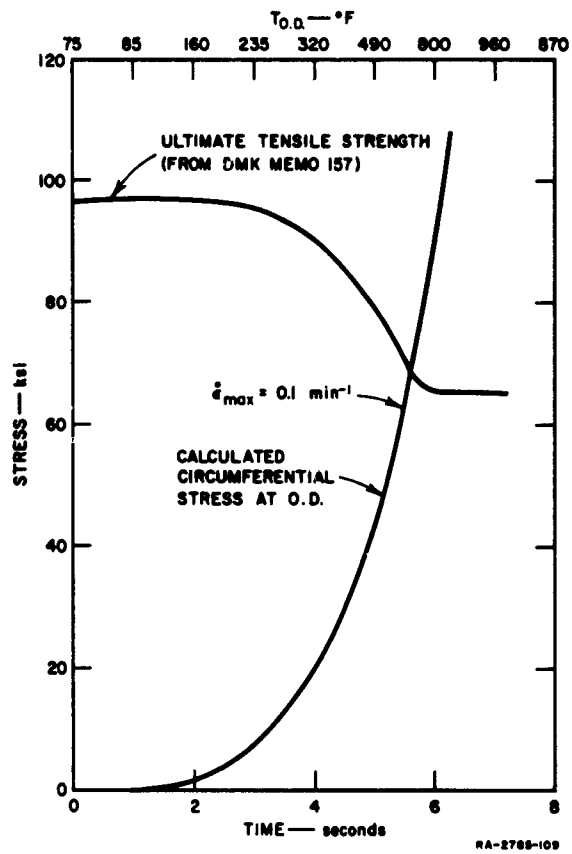

FIG. 14 STRESS AT OUTER SURFACE OF SPUN AND RECRYSTALLIZED TUNGSTEN CYLINDER (No. 7) vs. TIME AND O.D. TEMPERATURE

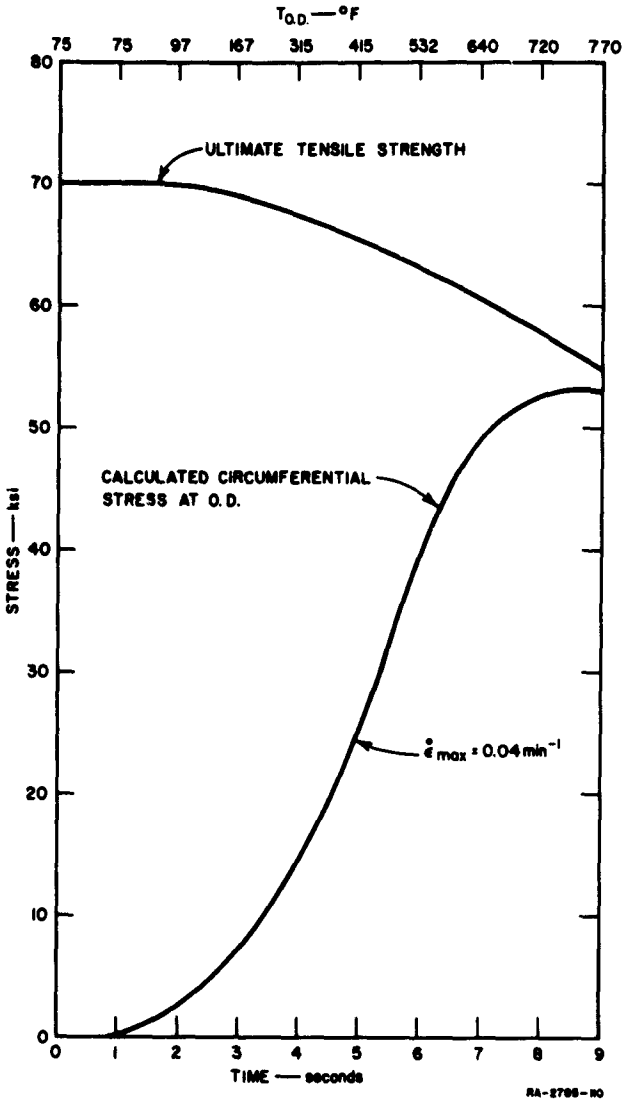

FIG. 15 STRESS AT OUTER SURFACE OF SILVER-INFILTRATED TUNGSTEN CYLINDER (No. Ag-7) vs. TIME AND O.D. TEMPERATURE

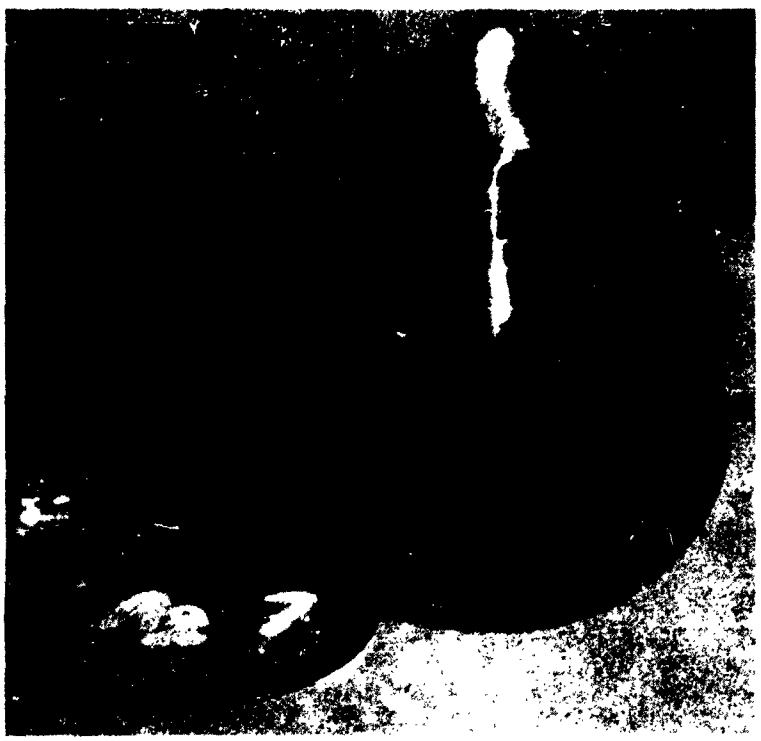

ZYGLOED ABOUT 2-1/2 x

RA-2786-1H

FIG. 16 SILVER-INFILTRATED TUNGSTEN SPECIMEN (Ag-7) SHOWING RADIAL THERMAL SHOCK CRACK

ZYGLOED ABOUT 2x

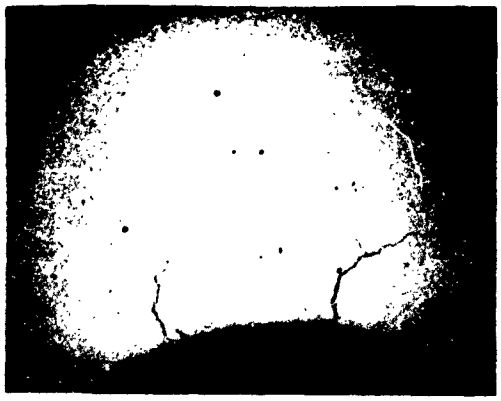

UNETCHED ABOUT 7x

RA-2706-112

FIG. 17 SILVER-INFILTRATED TUNGSTEN SPECIMEN SHOWING I.D. INITIATED CRACK NETWORK